


Towards more biologically plausible central-pattern-generator models

V. Baruzzi¹, M. Lodi¹, M. Storaice¹ and A. Shilnikov²

¹*Department of Electrical, Electronics and Telecommunication Engineering and Naval Architecture, University of Genoa, 16145 Genoa, Italy*

²*Neuroscience Institute and Department of Mathematics and Statistics, Georgia State University, Atlanta, Georgia 30303, USA*

 (Received 27 July 2021; revised 17 November 2021; accepted 19 November 2021; published 8 December 2021)

Central pattern generators (CPGs) are relatively small neural networks that play a fundamental role in the control of animal locomotion. In this paper we define a method for the systematic design of CPG models able to exhibit biologically plausible gait transitions by implementing short-term synaptic plasticity mechanisms. As a case study, we focus on a simple CPG for quadruped locomotion. By applying the proposed method, three of four standard quadruped gaits were correctly reproduced by the obtained CPG model, not only in terms of the alternating sequence of the limbs but also in terms of frequency, duty cycle, and phase lags.

DOI: [10.1103/PhysRevE.104.064405](https://doi.org/10.1103/PhysRevE.104.064405)

I. INTRODUCTION

Central pattern generators (CPGs) are small neural circuits that can produce rhythmic patterns of activity determining multiphase locomotion in diverse invertebrate and vertebrate animals [1], including in the absence of an external drive. The forms of locomotion that can be observed in animals vary in many ways in terms of exhibited gaits and posture, owing to the interplay of mechanical sensors and actuators (musculoskeletal system) and control (neural system). Mice, for example, can walk, trot, gallop, or bound [2,3]. This means that there must be mechanisms to change the synchronization patterns between the limbs and the limb segments during locomotion. So it may be reasonable to assume that rather than having multiple dedicated CPGs for such functions, there is a single multifunctional or multimodular CPG circuit that is versatile to coordinate all desired motor patterns [4].

The building module of most symmetric CPGs is the half-center oscillator, made of two reciprocally inhibited neurons (or neural pools) to produce antiphase activity patterns of alternating spike trains or bursts [5,6]. In Ref. [7] we extended this concept by proposing a *generalized* half-center oscillator (gHCO) made of the two neurons or pools (henceforth generically called *cells*) coupled reciprocally with inhibitory as well as with excitatory synapses. We demonstrated that such a dual connectivity allows for biologically plausible control of the phase lag between the cells, and thus switching between in-phase and antiphase by varying an external drive or current, without directly manipulating the synaptic conductance strengths. Indeed, from a biological standpoint, such conductance variations typically result from long-term synaptic plasticity; therefore, they cannot justify quick switches between the gaits. Such switches could be ascribed to short-term synaptic plasticity: Facilitation increases the probability of neurotransmitter release in a frequency-dependent manner [8], which was also observed and explored in swim CPGs of some sea slugs [9].

This paper is focused on quadruped locomotion. Detailed models of the mouse CPG were cataloged and examined in the last few years [10–12]. Here we explore the pos-

sibility of using the gHCO in the design of a minimalist CPG circuit that can stably produce gaits observed in four-limb animals. The schematic diagram in Fig. 1 is meant to illustrate two alternative strategies based on the interplay between network complexity and nonlinear dynamics of individual cells and synaptic properties. Our aim is to design a CPG with the simplest network architecture (i.e., minimalist functional topology)—containing only two gHCOs properly connected—by finding the parameters of cells and synapses through an optimization algorithm which accounts for physiological parameter ranges.

This feasibility study is based on three simple cornerstones: (i) short timescale gait transitions are triggered by short-term plasticity mechanisms; (ii) the CPG model is able to reproduce basic quadruped gaits with characteristic qualities; (iii) with bifurcation analysis we can calibrate key model parameters to meet specific gait features, following the guidelines in Ref. [13]. According to these premises, we further enhance the four-cell CPG model originally proposed in Ref. [13] by including the gHCO in its structure: In its simple circuitry, shown in Fig. 2, a pair of fore neurons and a pair of hind neurons represent essentially two gHCOs, whose cells are coupled by mixed synapses with different timescales. In what follows we will demonstrate the validity of our approach and the methods that let us reproduce three out of the four target gaits. We will also discuss some critical aspects to be accounted for in this updated CPG design.

II. FOUR-CELL CPG MODEL

Let us first introduce the abbreviations listed in Table I for various types of synapses employed in the four-cell CPG model.

The four-cell CPG model is shown in Fig. 2: Here each cell is modelled by the thalamic reticular burster [14,15] within the Hodgkin-Huxley (HH) framework (see Appendix A for a list of all fixed parameters and a description of their biological relevance). The dynamics of the membrane potential V_i and of the voltage-dependent state variables $\mathbf{y}_i \in \mathbf{R}^6$ (representing intracellular calcium concentration and gating variables) are

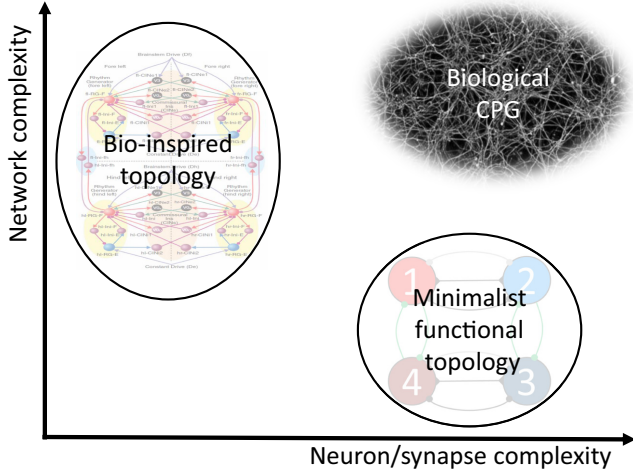


FIG. 1. Comparison diagram of two alternatives to model a biological CPG: (left) a detailed network architecture with simple functional units [10]; (right) simplest design with biologically plausible neural and synaptic models.

governed by HH-type ODEs ($i = 1, \dots, 4$)

$$\frac{d}{dt} \begin{bmatrix} V_i \\ \mathbf{y}_i \end{bmatrix} = \begin{bmatrix} -\sum_k I_k + I_i^{\text{syn}} \\ f(V_i, \mathbf{y}_i) \end{bmatrix}, \quad (1)$$

where the sum $\sum_k I_k$ includes the intracellular ionic currents, along with the current I_c used in this study as the control parameter; here $f(V_i, \mathbf{y}_i)$ is a logistic or sigmoidal function for the gating variables. This model demonstrates bursting activity for $I_c \in [-0.43, 0.13]$ ($\frac{\mu\text{A}}{\text{cm}^2}$), when the other parameters are set as in Appendix A [7]. The term I_i^{syn} groups together

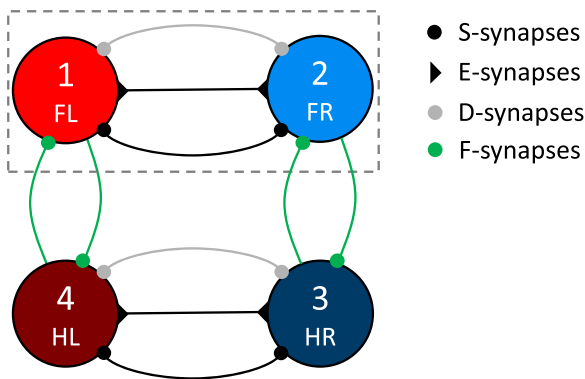


FIG. 2. CPG circuit of four coupled cells labeled as follows: FL and FR (fore-left and -right), HL and HR (hind-left and -right). The dashed box includes the gHCO that governs the fore limbs. The following symbols \blacktriangleright , \bullet , \circ , and \odot denote, respectively, the excitatory E and inhibitory S , F , and D synapses (see the table above). Each CPG cell controls flexor muscles regulating the swing phase of a limb, while D synapses simulate the actions of the neural populations (not explicitly represented in the given model) controlling the extensor muscles. The fore and hind gHCOs are coupled through ipsilateral F synapses.

TABLE I. Synapse types.

Synapse type	Abbreviation	Symbol
Fast excitatory	E	\blacktriangleright
Slow inhibitory	S	\bullet
Delayed fast inhibitory	D	\circ
Fast inhibitory	F	\bullet

the incoming synaptic currents,

$$I_i^{\text{syn}} = \sum_{j=1}^4 \{ g_{ij}^E [E^E - V_i(t)] s_j^E + g_{ij}^S [E^S - V_i(t)] s_j^S + g_{ij}^D [E^S - V_i(t - \delta)] s_j^D + g_{ij}^F [E^S - V_i(t)] s_j^F \}, \quad (2)$$

where E^k ($k = E, S$) represents the reversal potentials for excitatory ($k = E$) and inhibitory ($k = S$) synapses, $0 \leq s_j^k(V_i, t) \leq 1$ ($k = E, S, D, F$) describes the neurotransmitter release rate of the synapse, g_{ij}^k ($k = E, S, D, F$) is the maximal synaptic conductance or weight, while δ is the time delay imposed for D -type synapses.

The S synapses are described by a first-order kinetic model [16–19],

$$\begin{aligned} \frac{ds_j^S}{dt} &= \alpha (1 - s_j^S) f_\infty^S(V_j) - \beta s_j^S, \\ f_\infty^S &= \frac{1}{1 + e^{-v(V_j - \theta^S)}}, \end{aligned} \quad (3)$$

where θ^S is the synaptic threshold, and α and β are coefficients determining the exponential raise and decay rates, respectively: The greater the α (β) values, the faster the raise (decay) rates of s_j^S after the presynaptic voltage V_j goes over (under) θ^S . The fast E -, D -, and F -type synapses are modeled using the fast threshold modulation approach [16,20], $s_j^k = f_\infty^k(V_j)$ ($k = E, D, F$).

Let us argue our motivation for choosing these synapses in the four-unit CPG model under consideration, where each neural unit controls the flexor regulating the swing phase of the corresponding limb. Some of these synapses result from the functional reduction of the detailed, 40-cell mouse locomotion CPG proposed in Ref. [10] down to the 4-cell circuit initially introduced in Ref. [21]. In particular, the F synapses were introduced to replace inhibitory interneuron populations that do not introduce significant delay, and the D synapses simulate the delayed action of the neuron groups controlling the extensor muscles. Moreover, the nonlinear interplay of both fast-excitatory and slow-inhibitory synapses is pivotal to devise our (simple yet functional and flexible) CPG network: S and E synapses [7] are crucial to model the effect of short-term synaptic plasticity, as discussed below.

By fitting its key parameters, we aim to make this minimalist 4-cell CPG able to generate all four mouse gaits: walk (W), trot (T), gallop (G), and bound (B). Each gait has specific quantitative features [2,3] such as the frequency (f) and duty cycle (d) of each rhythmic pattern driving a limb and the phase

TABLE II. Quadruped gait features [2,3].

Gait	f (Hz)	d	Δ_{12}	Δ_{13}	Δ_{14}
Walk (W)	[2 4]	<0.4	0.5	0.75	0.25
Trot (T)	[4 9]	[0.4 0.51]	0.5	0	0.5
Gallop (G)	[9 10]	>0.51	0.1	0.5	0.6
Bound (B)	[10 12]	>0.51	0	0.5	0.5

lags,¹ Δ_{12} , Δ_{13} , Δ_{14} , between the driving signal generated by the reference cell 1 and the ones produced by the other three cells. These features are summarized in Table II. The spatiotemporal patterns of each mouse gait are depicted in Fig. 3. Note that walk and trot require that the fore (and hind) cells burst in antiphase at low burst frequencies, whereas during bound they become synchronized in phase with higher burst frequencies.

The thalamic reticular neuron model in isolation exhibits [7] (see Fig. 4):

(i) high-frequency bursting with low intraburst spike frequency and high duty cycle d at small I_c values;

(ii) slow bursting with high intraburst spike frequency and low duty cycle d at greater I_c values.

We define a threshold V_t (gray horizontal line in Fig. 4) to calculate the duty cycle d as the ratio between the time interval in which $V_i(t) > V_t$ within a period (red interval) and the period (red plus blue intervals). Unlike fast synapses, which do not depend on spike frequency, we need to calibrate slow synapses in such a way that the spiking frequency of the burster enables postsynaptic potential (PSP) summation.² It was shown in Ref. [7] that such a summation may result in in-phase synchronization at low intraburst spike frequency but give rise to antiphase synchronization at high intraburst spike frequency of the gHCO cells with mixed slow (fast) inhibitory (excitatory) synapses. In particular, the key parameters α , β , and θ^S , regulating the dynamics of S synapses, can be calibrated to ensure that the mean synaptic activation \bar{s}_j^S changes significantly when the presynaptic spike frequency varies. In other words, we want to have small \bar{s}_j^S values at low spike frequency and substantially larger \bar{s}_j^S values at higher spike frequencies. On the contrary, the mean activation of the E synapse \bar{s}_j^E is not affected by spike frequency variations. When the synaptic weights are properly balanced, this leads to excitation prevailing over inhibition at low spike frequency, which makes the gHCO neurons synchronize in-phase. By contrast, growing inhibition prevails over excitation at high spike frequencies, forcing the neurons to burst in alternation. Therefore, variations of the intraburst spike frequency, being indirectly regulated by the external drive I_c , can trigger transitions from in-phase to antiphase bursting and vice versa. This

¹The phase lag Δ_{ij} (defined on mod 1) between burst initiations in the cells i and j allows quantifying the phase-locked states produced by the CPG. In case of synchronous or in-phase bursters $\Delta_{ij} = 0$ or 1, equivalently. Bursting in alternation with $\Delta_{ij} = 0.5$ is referred to as antiphase.

²Temporal PSP summation in a postsynaptic cell is hypothesized to get triggered by increasing frequencies of action potentials in the presynaptic cell [22].

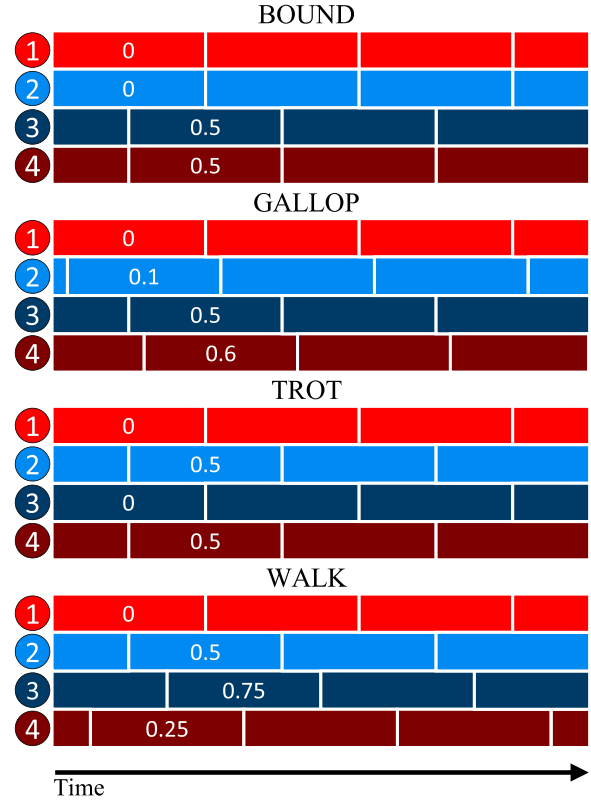


FIG. 3. Spatiotemporal patterns of the four mouse gaits (with the colors matching the cells in Fig. 2): bound, gallop, trot, and walk with the characteristic phase lags (as listed in Table II) between the reference cell 1 and the other three cells of the CPG.

explains how the interplay of E and S synapses gives rise to short-term synaptic plasticity in our model. A convenient way to illustrate phase transitions in the gHCO is to plot the locked phase lag Δ_{12} against I_c in a bifurcation diagram. We remark that simulations of the gHCO have to be performed with various initial conditions of the state variables, to detect for which ranges of I_c bi- or multistability over different Δ_{12} values is present, if any. A monostable gHCO (or CPG circuit) stably yields the same phase lags Δ_{12} (and Δ_{13} , Δ_{14}) locked regardless of initial conditions and without hysteresis effects due to I_c being increased or decreased.

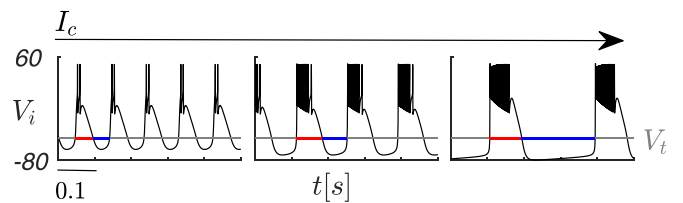


FIG. 4. Voltage traces of the isolated burster (A1) at three different I_c values: -0.43 ($\frac{\mu\text{A}}{\text{cm}^2}$) (left panel), -0.15 ($\frac{\mu\text{A}}{\text{cm}^2}$) (center), and 0.13 ($\frac{\mu\text{A}}{\text{cm}^2}$) (right); the other parameters are set as listed in Appendix A. The threshold V_t (gray horizontal line) is used to calculate the duty cycle d as the ratio between the red interval and the period (red plus blue intervals).

III. PARAMETER FITTING TO QUADRUPED GAIT FEATURES

Let us reiterate that our objective is to devise a CPG model that can exhibit intrinsic short-term synaptic plasticity in the form of facilitation (without any changes in synaptic weights) and is able to generate all desired gaits and trigger gait transitions. To achieve this goal, we first need to evaluate and fix a range of several cellular and synaptic parameters that stably yield the four quadruped gaits with the realistic features listed in Table II. This task is challenging, mainly due to the high number of parameters and their balance and to the constraints imposed on the overall model performance.

In what follows, we will define and outline our strategy (summarized in Fig. 5) that further exploits the design methods proposed previously in Refs. [7,13] to systematically calibrate both neuronal and synaptic parameters. This strategy includes several steps discussed in detail below. In brief, the initial steps from 0 through 5 in Fig. 5 deal with the steady-state behaviors of the network, while possible transitions (transient dynamics) are examined at the final step 6. It should be quite clear from the beginning that, due to its high dimensionality, the complex problem of parameter setting cannot be addressed by a monolithic brute-force approach based on performing exhaustive search.

Therefore, to solve this puzzle, the original problem should be hierarchically subdivided into consecutive simpler steps. However, the dynamics of the complete CPG network results from the interplay of the dynamics of the four individual cells coupled by mixed synapses with different timescales. Therefore, given that the correct behavior of the complete CPG is not guaranteed *a priori*, the previously found results should not be tabulated but revisited and verified *a posteriori*, as suggested by the last two steps of the proposed strategy.

Step 0—Fixing the key synaptic parameters: This lets us reduce the dimension of the set of parameters to be optimized, based on preliminary considerations (see Appendix B for the set values). This includes the time delay δ of the D synapses, which is set to be half of the bursting period of the presynaptic neuron since we assume that flexor and extensor cells are activated in antiphase. The synaptic thresholds, θ^E , θ^D , and θ^F , of all fast synapses are set the same so that their strength does not change with spike frequency variations [7]. The parameter ν is set the same for all synapse types [7]. Also the weights g_{ij}^D of the delayed D synapses, which are an order of magnitude weaker than g_{ij}^S of the S synapses according to Ref. [13], are set all equal. In addition, following Ref. [13], the ratios g_{41}^E/g_{14}^E and g_{32}^E/g_{23}^E (i.e., the ratios of the weights of fore-to-hind and hind-to-fore coupling) are set the same.

Step 1—Single cell: Its temporal scaling is performed through the parameter ξ so that the values of the burst frequency f , obtained by varying I_c in the burst region, span the range required to model all gaits as listed in Table II. The reference voltage V_r , used to calculate the duty cycle d , is consequently adjusted to obtain the desired values of d . The result of this step is a pair of bifurcation diagrams (see Fig. 6) showing how f (bottom panel) and d (top panel) are controlled by the drive I_c across all four gaits, labeled as B[ound], G[allop], T[rot], and W[alk] in the color-coded intervals.

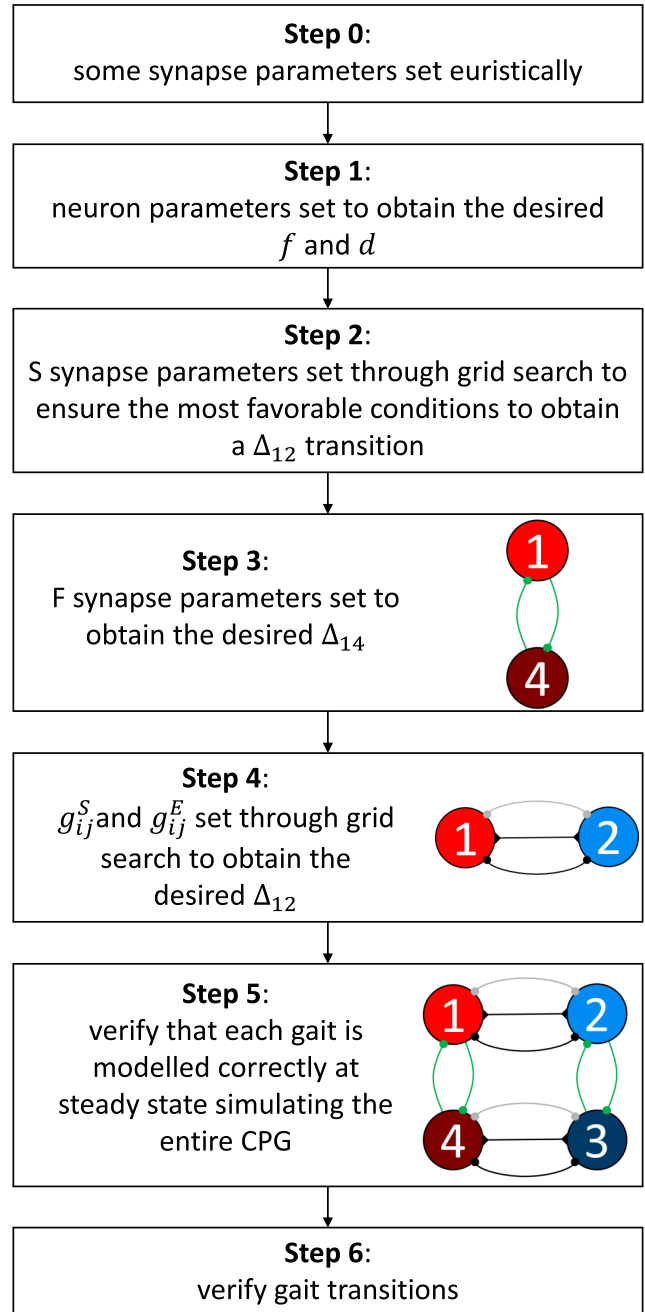


FIG. 5. Flowchart summarizing the design strategy proposed: Steps 0 through 5 focus on the steady-state dynamics of the network, while step 6 verifies the transitions between gaits.

Step 2—S-type synapses: Their key parameters, exponential factors α , β , and synaptic threshold θ^S , are identified through grid search to meet the following two conditions:

(i) the mean synaptic activation \bar{s}_j^S (evaluated over the burst period) is maximized (minimized) at the right (left) endpoint of the I_c range $[-0.43, 0.13] \frac{\mu A}{cm^2}$;

(ii) ratio $\psi = \bar{s}_j^S/\bar{s}_j^E$ of mean inhibition and excitation influx is monotonically increased with increasing I_c .

The above simple constraints ensure the most favorable conditions to obtain the transition of the phase lag Δ_{12} from in-phase to antiphase as I_c is varied, provided that the weights

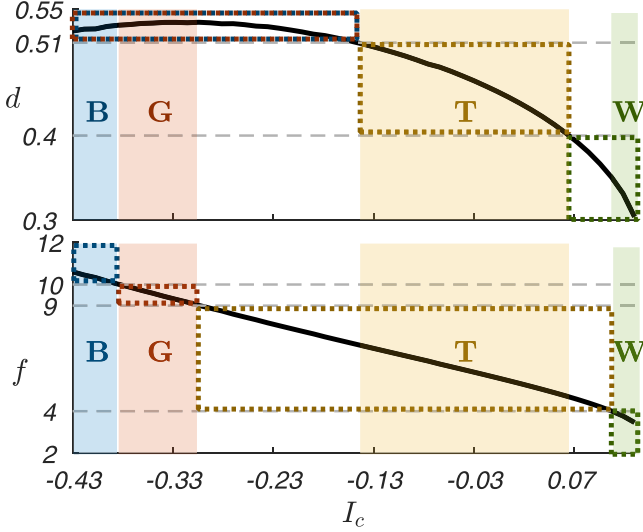


FIG. 6. Duty-cycle d and bursting frequency f (Hz) of the neuron model (to be compared to d and f in Table II) against I_c ($\mu\text{A}/\text{cm}^2$). In both panels the horizontal dashed gray lines mark the d or f ranges corresponding to each gait (see Table II); the dotted rectangles mark the corresponding I_c intervals for d and f . Observe that there is no threshold separating B and G duty-cycle intervals as their ranges overlap. Colored areas highlight the I_c intervals suitable (in terms of frequency and duty cycle) for each gait, as obtained from the intersection of the conditions for both features: B (blue), G (red), T (yellow), and W (green).

g_{ij}^S and g_{ij}^E (set in step 4) are properly balanced. The result is illustrated in Fig. 7.

Step 3—Combined fore and hind gHCOs: They are coupled in a pairwise manner by the inhibitory F synapses through cells 1 and 4 and through cells 2 and 3. Consider ΔI_c as the difference between the I_c values driving the fore and hind cells: $I_{c1/2} + \Delta I_c = I_{c4/3}$, respectively. The bursting dynamics of the subnetwork (cells 1 and 4 or, equivalently cells 2 and 3) are simulated over a dense grid of I_c and ΔI_c values (within the ranges determined in step 1), matching the weights g_{ij}^E (whose ratio is fixed in step 0) to identify the correct fore or hind phase lags (Δ_{14} and Δ_{23}) of the targeted gaits. The outcome of this simulation step is a set of $(I_c, \Delta I_c)$

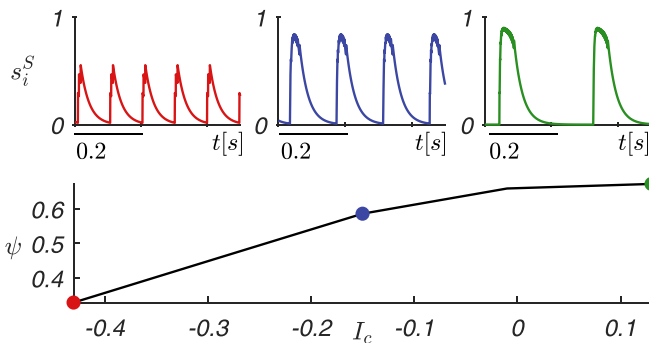


FIG. 7. Bottom: The ratio ψ between mean inhibition or excitation influx through the S and E synapses, plotted against the external drive I_c ($\mu\text{A}/\text{cm}^2$). Top insets showing steady-state time plots of $s_i^S(t)$ at $I_c = -0.43$ (left panel), -0.15 (center), and 0.13 (right).

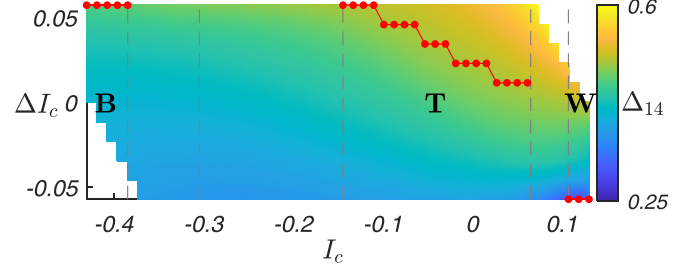


FIG. 8. Color map of the phase lag Δ_{14} over a grid of I_c ($\mu\text{A}/\text{cm}^2$) and ΔI_c ($\mu\text{A}/\text{cm}^2$) values, for fixed g_{ij}^E (see Appendix for numeric values). Red dots mark $(I_c, \Delta I_c)$ pairs that yield Δ_{14} values closest to the desired ones for bound, trot and walk in the proper I_c intervals. Appropriate values of Δ_{14} to model gallop are not achieved in the corresponding I_c interval. Red solid lines denote the piecewise-linear function $\Delta I_c(I_c)$ that interpolates the found $(I_c, \Delta I_c)$ pairs for bound, trot and walk.

pairs that yield the desired Δ_{14} values for each gait within the proper I_c intervals, see the color map shown in Fig. 8. With this map, a function $\Delta I_c(I_c)$ can be defined through a piecewise-linear interpolation of the identified $(I_c, \Delta I_c)$ pairs. Such a function is used to properly drive the control action through I_c for all the CPG cells and obtain the desired Δ_{14} .

Step 4—Intra-gHCO synapses: The balanced weights g_{ij}^S and g_{ij}^E of the intra-gHCO inhibitory and excitatory synapses are identified through a dense grid search so that they guarantee the desired steady-state Δ_{12} phase lag for each gait within the I_c intervals (determined in step 1).

Step 5—Full CPG model: It is simulated with the parameter values determined in the previous steps to verify that, as a whole, it produces all established gaits regardless of initial conditions of the four cells.

Step 6—Gait transitions: They are verified while I_c is varied.

IV. RESULTS: MODELING THE GAITS

The bifurcation analysis of our CPG model was performed using the toolbox CEPAGE [23], with the parameter values summarized in the Appendices. Step 3 lets us identify the synaptic parameters to stably maintain the desired phase lag Δ_{14} near the target values in the bound, trot, and walk regions. We note, however, that the value of Δ_{14} for the gallop gait, which should be near 0.6, was not as accurately reproduced as the targeted phase lags for the other gaits. This is evident in Fig. 8, showing the piecewise-linear function $\Delta I_c(I_c)$ (in red) that yields the correct Δ_{14} values for bound, trot, and walk. We also examined an extended ΔI_c range and found that higher differences in the I_c values for fore and hind cells would cause self-sustained and irregular oscillations of Δ_{14} instead.

According to step 4, we performed a grid search over g_{ij}^S and g_{ij}^E values to determine which weight combinations give the desired Δ_{12} for each gait. Because modeling the gallop gait is precluded by the result of step 3, our focus was on modeling the three remaining gaits: bound, trot and walk. For each of the corresponding I_c intervals identified in step 1, we examine a fixed I_c value representative of the gait by prioritizing structural stability of the rhythm generation, i.e.,

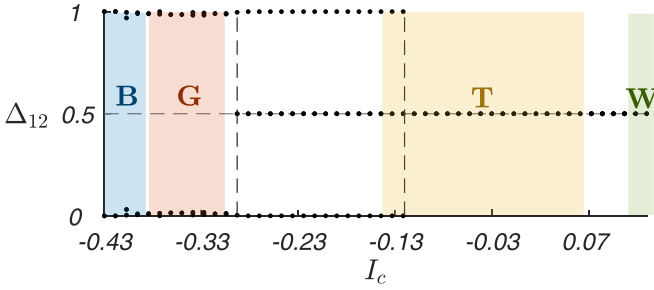


FIG. 9. Bifurcation diagram that shows the phase lag Δ_{12} at steady state of the cells in the gHCO against I_c ($\mu\text{A}/\text{cm}^2$). Colored rectangles highlight the I_c intervals suitable for each gait determined in step 1: B (blue), G (red), T (yellow), and W (green). The vertical dashed lines indicate the parameter range where the CPG circuit becomes bistable.

by choosing I_c sufficiently far from adjacent intervals or from transition values. For each weight pair and identified I_c value, we simulated the gHCOs with initial conditions close to 0 and 0.5 (respectively, in-phase and antiphase states) using the following validation criteria: A g_{ij}^S - g_{ij}^E pair is considered valid if it warrants a Δ_{12} phase lag close enough to the tabulated values (see Table II) regardless of initial conditions. Among all such combinations, we selected the (g_{ij}^S, g_{ij}^E) pair that corresponds to the best bifurcation diagram, guaranteeing the target Δ_{12} values for the gaits, and no multistability for the broadest stretch in the I_c intervals determined in step 1. This bifurcation diagram is shown in Fig. 9. It evidences that the I_c range corresponding to the bistable CPG lies almost completely outside of the parameter intervals determined in step 1, thus barely interfering with the network functionality in the trot region. On the other hand, the presence of multistability is indicative of the hysteresis associated with gait transitions, which is a well-known phenomenon in animal locomotion reported in numerous experimental studies [24,25]. As an additional consideration, we point out that no weight combinations yielded the desired Δ_{12} value for gallop, unlike other gaits, thus confirming the difficulty in modeling this gait.

The complete CPG was next simulated to test its rhythm-generation, according to step 5. One can observe from Figs. 10–12 that the proposed CPG-circuit produces, respectively, bound, trot, and walk correctly with the desired Δ_{12} , Δ_{13} , and Δ_{14} phase lags. The phase lags between all cells for all gaits are in agreement with the results obtained in steps 3 and 4, confirming the reliability of the proposed design method. Note that, due to reciprocal interactions, the corresponding frequency f and duty cycle d of the network cells differ from those recorded in the isolated ones for the same I_c values. Stronger synaptic coupling results in greater f and d deviations from the values in isolation. Note, however, that lower synaptic weights would not satisfy the requirements imposed in steps 3 and 4. The shift from the expected value of d can be at least partially corrected *a posteriori* by acting on the reference voltage V_i used to calculate d , which does not influence any other aspect in the CPG dynamics.

Last, according to step 6, we verified the transient behavior of the CPG by varying I_c and ΔI_c following the piecewise linear function (shown in red) in Fig. 8 and observing the

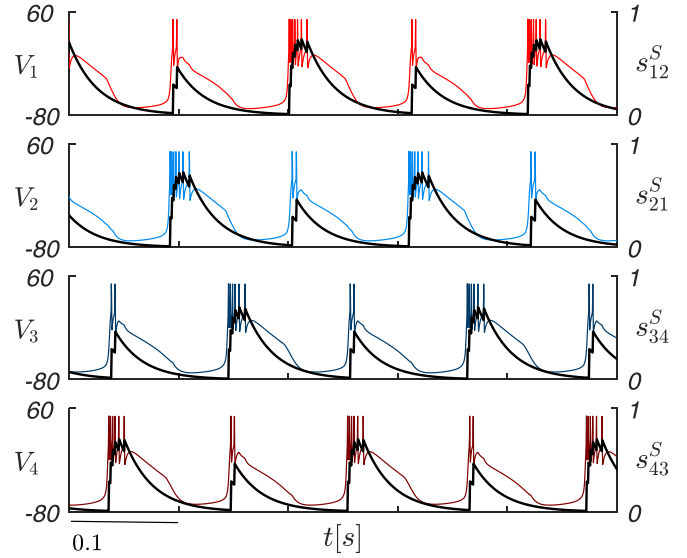


FIG. 10. Steady-state bound. Membrane voltage V_i (mV) of each of the four neurons (colors as in Fig. 2) and synaptic activation s_i^S of the efferent S synapse (black lines).

transitions between gaits. As can be seen in Fig. 13, all transitions happen promptly (in less than 2 s) and smoothly. However, when transitioning from trot to walk, we observe that, during a time transient in the order of tens of seconds after the transition, neurons 1 and 2 occasionally skip a burst, momentarily disrupting the alternation sequence, as shown in Fig. 14. To identify the cause of this behavior, we examined the influence of inhibitory and excitatory synapses separately. We found that the same phenomenon still occurs with the E-type synapses silenced, for weights of the S -type synapses g_{ij}^S in the order of magnitude determined in step 4. Such a behavior was not observed for values of g_{ij}^S decreased of more than two orders of magnitude. This again suggests that lower

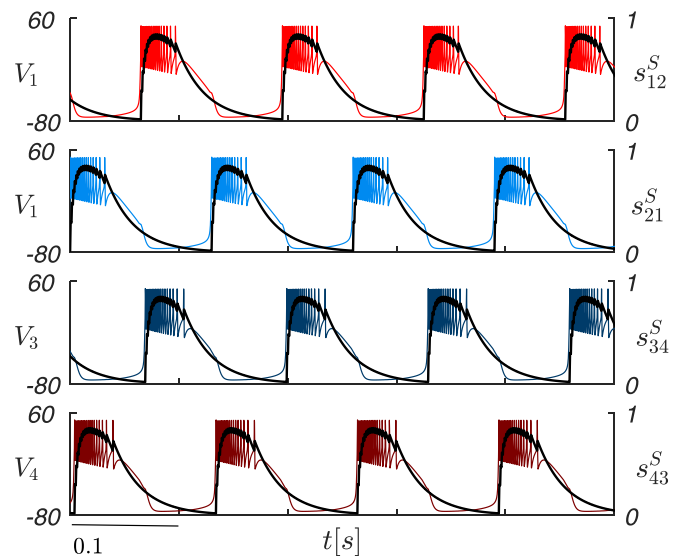


FIG. 11. Steady-state trot. Membrane voltage V_i (mV) of each of the four neurons (colors as in Fig. 2) and synaptic activation s_i^S of the efferent S synapse (black lines).

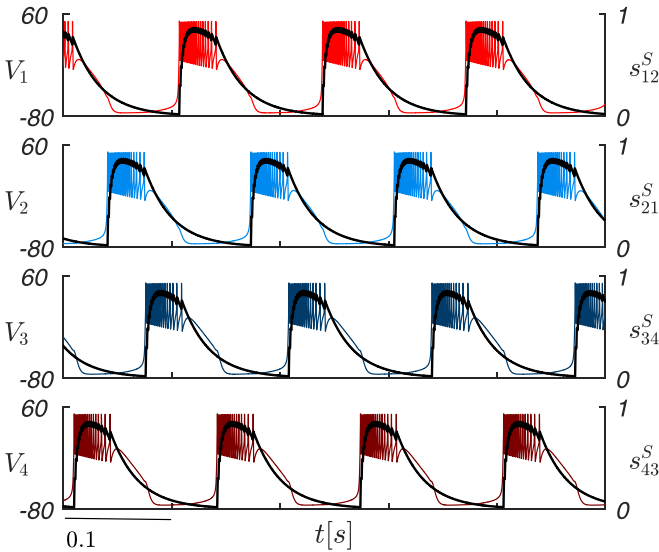


FIG. 12. Steady-state walk. Membrane voltage V_i (mV) of each of the four neurons (colors as in Fig. 2) and synaptic activation s_{ij}^S of the efferent S synapse (black lines).

synaptic weights would be less problematic in terms of any unwanted behavior caused by the interplay of the different dynamics within the network. The definition of more efficient learning strategies (to allow better exploring of the high-dimensional parameter space) along with the use of different synapse models (to better meet the design requirements) is a main priority in future developments of our design method, that will be discussed in the following section.

V. DISCUSSION AND CONCLUSIONS

In this paper, we proposed a design strategy to devise CPG models according to our minimalist-functional-topology approach (see Fig. 1), using a simple network structure while focusing on realistic modeling of nonlinear cellular and synaptic dynamics to account for short-term synaptic plasticity. The resulting CPG model can reproduce the sought locomotion patterns of the mouse rather well and could have a potential in robotics applications. Indeed, engineering the modern mobile robots requires a knowledge of a section of the theoretical biology that is relating to the dynamics of CPGs [26,27]. Generally speaking, the choice between a bio-inspired-topology and a minimalist-functional-topology approach (or an intermediate recipe with a different mix of levels of abstraction for network structure and elements) is driven by the specific application or designer interest.

The proposed design or learning strategy relies on tuning the parameters of a model whose topology is given *a priori* through extensive simulations and optimizations. The strategy described in the paper hierarchically subdivides the high-dimensional problem of parameter setting into consecutive simpler steps, each one giving as output the optimal subset of parameter values to be used as footprint for the following step. Dividing the problem in steps, not only makes it approachable in terms of dimensionality reduction, but also gives insight into the role of each subsystem and its interplay with other model elements. The success of each step depends of course

on the neuron and synapses models adequacy in fulfilling the requirements for the target gaits. We also remark that the dynamics of the final CPG network depends on the interplay of all model elements; therefore, the correct behavior of the complete CPG cannot be guaranteed *a priori* and should be verified and revised *a posteriori*, as suggested by the last two steps of the proposed strategy. Moreover, the strategy described in the paper is not recursive in nature. Recursion can be nonetheless integrated into this learning strategy by replacing steps 4 and 5 with steps 4B and 5B as in Fig. 15. Starting from null gHCO synaptic weights ($g_{ij}^S = g_{ij}^E = 0$), in step 4B the weights g_{ij}^S (identical, to maintain the gHCO symmetry) are increased until the CPG is able to produce the desired gaits with Δ_{12} close to 0.5 (trot and walk, in the considered case) for sample values of I_c and ΔI_c representative of the gaits, regardless of initial conditions. If the obtained CPG is not able to model the desired gaits with Δ_{12} close to 0 (bound, in our case), step 5B is performed. In step 5B the weights g_{ij}^E (identical) are increased until the CPG is able to produce the desired gaits with Δ_{12} close to 0 for sample values of I_c and ΔI_c representative of the gaits, regardless of initial conditions. If the new CPG is not able to model the desired gaits with Δ_{12} close to 0.5, then step 4B is repeated.

The steps are reiterated until all gaits are modeled correctly. Since the success of the strategy is not guaranteed *a priori*, the iterations should be stopped when the weights reach unrealistically high values.

Usually, the outcomes of both the original and the alternative strategy are equivalent, since both strategies will yield a gHCO weight pair g_{ij}^S, g_{ij}^E that leads to excitation prevailing at low spike frequency (causing the neurons of the gHCO to synchronize) and inhibition prevailing at high spike frequency (causing the neurons to alternate). Steps 4B and 5B are less computationally demanding than the grid search in step 4 of the original strategy but do not span the complete parameters domain, possibly leading to a local minimum. Moreover, the grid search in step 4 can produce more than one valid weight pair, giving the possibility of selecting the most favorable pair based on additional considerations on the bifurcation diagram. For example, one could select the bifurcation diagram where no multistability is present for the longest stretch in the I_c intervals determined in step 1.

Future advances in this line of work will focus on integrating machine learning methods in the CPG design strategy, to further improve its efficiency and reliability. An example that goes in this direction is the design strategy for a spike-based hexapod CPG that employs supervised learning, proposed in Ref. [28]. The strategy has the advantage of being based on a very simple learning rule but has the drawback of being structurally bounded to learn at most three given gaits and does not take into consideration additional gait characteristics other than the legs activation sequence.

The proposed bio-inspired 4-cell CPG is indeed able to model gait transitions in a biologically plausible way, through varying external currents only, while synaptic conductances and time constants remain fixed. Following the proposed design strategy, we reproduced correctly three desired gaits (bound, trot, and walk) of the four, as well as smooth and prompt transitions between them. We failed to find the parameter values to obtain gallop, which confirms the difficulty

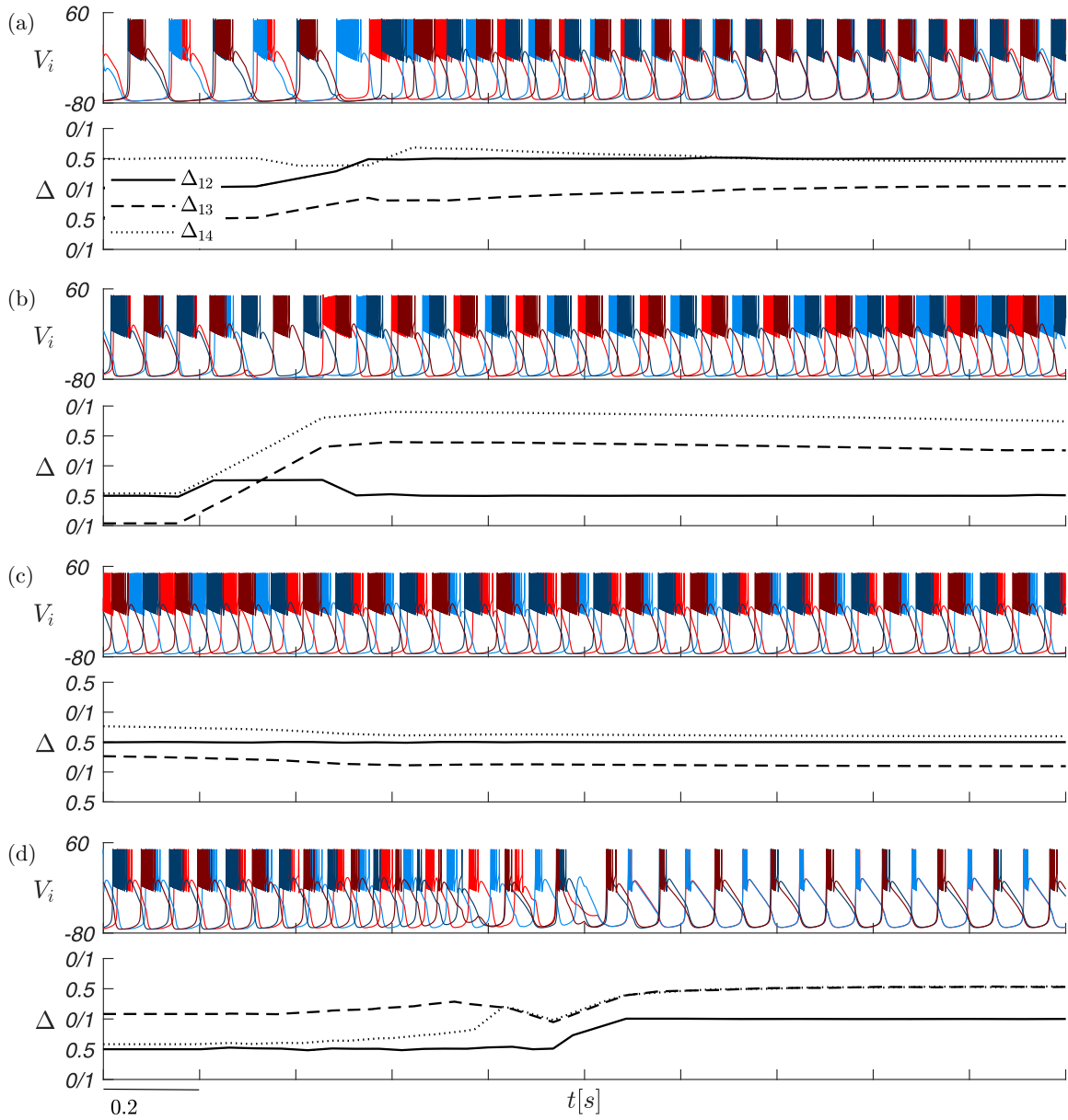


FIG. 13. Membrane voltage V_i ($i = 1, 2, 3, 4$) of the four neurons (colors as in Fig. 2) and phase lags Δ_{1j} ($j = 2$ solid line, $j = 3$ dashed line, $j = 4$ dotted line) during the transitions between bound and trot (a), trot and walk (b), walk and trot (c), and trot and bound (d). The transitions are obtained by varying the values of I_c and ΔI_c following the red piecewise-linear function shown in Fig. 8.

in obtaining the corresponding phase lag Δ_{12} using fast excitatory synapses and slow inhibitory synapses in the given CPG. This observations suggest the need of revisions of the network to remedy this issue in future work. For example, one option is to consider a network configuration where each cell is composed of a spiking and a bursting neuron to factually decouple the intraburst spike frequency and the burst frequency of the cell. Then, fast inhibitory synapses and slow excitatory synapses in such a CPG could provide the desired phase lag Δ_{12} more affordably.

Other improvements could include adopting different network connectivity and other dynamical models of neurons and

slow synapses to warrant a greater contrast in mean activation at low and high spiking frequency values. This should potentially facilitate the demanding and complex process of parameter optimization.

ACKNOWLEDGMENT

A. Shilnikov acknowledges a partial funding support from the Brain&Behaviors pilot grant.

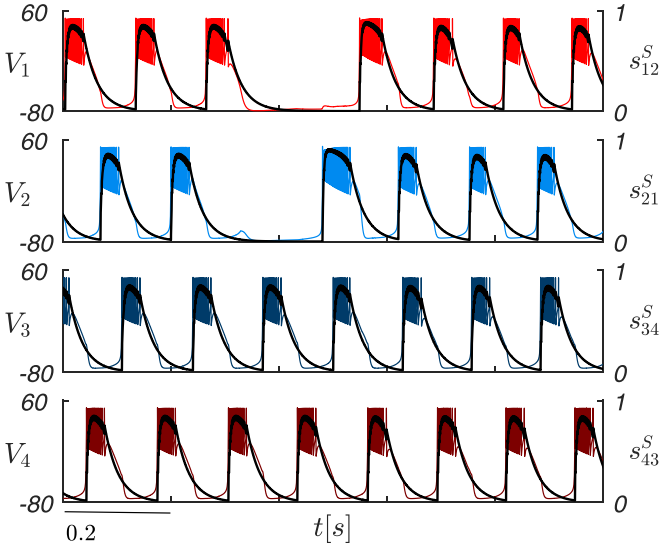


FIG. 14. Fragment of the time interval where neurons 1 and 2 skip a burst after the transition from trot to walk. Membrane voltage V_i (mV) of each of the four neurons (colors as in Fig. 2) and synaptic activation s_i^S of the efferent S synapse (black lines).

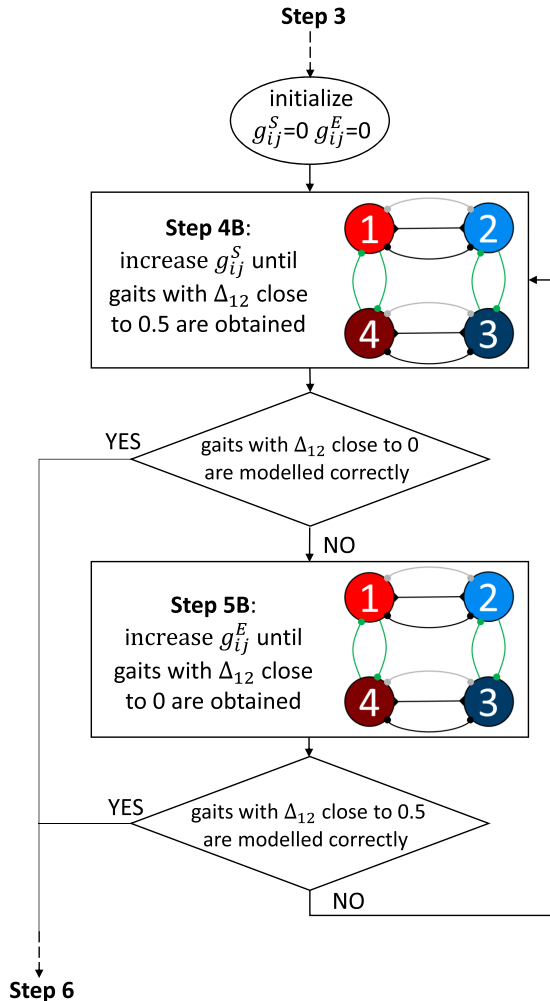


FIG. 15. Recursive flowchart that summarizes the alternative steps 4B and 5B.

APPENDIX A: THALAMIC RETICULAR NEURON MODEL

The thalamic reticular neuron model [14,15] is defined by the following state equations:

$$\begin{aligned} \xi \frac{dV}{dt} &= \frac{-I_T - I_L - I_{Na} - I_K - I_c + I^{\text{syn}}}{C}, \\ \xi \frac{dCa}{dt} &= -\frac{kI_T}{2FD} - \frac{K_T Ca}{Ca + K_d}, \\ \xi \frac{dy}{dt} &= \frac{y^\infty - y}{\tau_y}, \quad y = \{h, m, n, m_T, h_T\}, \end{aligned} \quad (\text{A1})$$

where V is the membrane potential of the neuron, Ca is the intracellular calcium concentration, and y is the generic gating variable. The only difference with respect to the original model is the presence of the dimensionless coefficient ξ , which scales the time variable t and thus determines the burst frequency f (obtained in step 1 by varying I_c in the burst region) so that it spans the range required to model the desired gaits. The ion currents I_T (calcium), I_{Na} (sodium), I_K (potassium), and I_L (leakage) evolve according to the following equations:

$$\begin{aligned} I_T &= g_{Ca} m_T^2 h_T (V - E_{Ca}), & I_L &= g_L (V - E_L), \\ I_{Na} &= g_{Na} m^3 h (V - E_{Na}), & I_K &= g_K n^4 (V - E_K), \end{aligned}$$

which depend on V , Ca , and on the gating variables h (inactivation variable of the Na^+ current), m (activation variable of the Na^+ current), n (activation variable of the K^+ current), m_T (activation variable of the low-threshold Ca^{2+} current), and h_T (inactivation variable of the low-threshold Ca^{2+} current). All gating variables evolve according to the differential equations written above for y , where

$$\begin{aligned} y^\infty &= a_y / (a_y + b_y), & \tau_y &= 1 / (a_y + b_y) \quad (y = \{h, m, n\}) \\ a_h &= 0.128 e^{\frac{17-V}{18}}, & b_h &= \frac{4}{e^{-0.2(V-40)} + 1}, \\ a_m &= \frac{0.32(13-V)}{e^{0.25(13-V)} - 1}, & b_m &= \frac{0.28(V-40)}{e^{0.2(V-40)} - 1} \\ a_n &= \frac{0.032(15-V)}{e^{0.2(15-V)} - 1}, & b_n &= 0.5 e^{\frac{10-V}{40}} \\ m_T^\infty &= \frac{1}{1 + e^{-\frac{V+52}{7.4}}}, & \tau_{mT} &= 0.44 + \frac{0.15}{e^{\frac{V+27}{10}} + e^{-\frac{V+102}{15}}}, \\ h_T^\infty &= \frac{1}{1 + e^{\frac{V+80}{5}}}, & \tau_{hT} &= 62.7 + \frac{0.27}{e^{\frac{V+48}{4}} + e^{-\frac{V+407}{50}}}. \end{aligned}$$

In the above equations, the leakage current I_L has conductance $g_L = 0.05$ ($\frac{\text{mS}}{\text{cm}^2}$) and reversal potential $E_L = -78$ (mV); I_{Na} and I_K are the fast Na^+ and K^+ currents responsible for the generation of action potentials, with conductances $g_{Na} = 100$ ($\frac{\text{mS}}{\text{cm}^2}$) and $g_K = 10$ ($\frac{\text{mS}}{\text{cm}^2}$) and reversal potentials $E_{Na} = 50$ (mV) and $E_K = -95$ (mV); I_T is the low-threshold Ca^{2+} current that mediates the rebound burst response, with conductance $g_{Ca} = 1.75$ ($\frac{\text{mS}}{\text{cm}^2}$) and reversal potential $E_{Ca} = k_0 \frac{RT}{2F} \log(\frac{Ca_0}{Ca})$; I^{syn} is the synaptic current Eq. (2) in the paper. When the control current I_c is in the range $[-0.43, 0.13]$ ($\frac{\mu A}{\text{cm}^2}$) the neuron exhibits bursting behavior. The other parameters

TABLE III. Parameter values set in each step.

Parameter	Value	Parameter	Value
		Step 0	
θ^E	-50 mV	g_{ij}^D	$0.0119g_{ij}^S$
θ^D	-50 mV	g_{41}^F/g_{14}^F	2.3327
θ^F	-50 mV	g_{32}^F/g_{23}^F	2.3327
ν	10 mV^{-1}	δ	Half of burst period
		Step 1	
ξ	3.0303	V_r	-50 mV
		Step 2	
α	0.7543 kHz	θ^S	17.5 mV
β	0.0391 kHz		
		Step 3	
g_{41}^F	0.0048 nS/cm ²	g_{32}^F	0.0048 nS/cm ²
g_{14}^F	0.0111 nS/cm ²	g_{23}^F	0.0111 nS/cm ²
		Step 4	
g_{12}^S	0.1207 nS/cm ²	g_{12}^E	0.0052 nS/cm ²
g_{21}^S	0.1207 nS/cm ²	g_{21}^E	0.0052 nS/cm ²
g_{34}^S	0.1207 nS/cm ²	g_{34}^E	0.0052 nS/cm ²
g_{43}^S	0.1207 nS/cm ²	g_{43}^E	0.0052 nS/cm ²

are set as follows: $C = 1$ ($\frac{\mu\text{F}}{\text{cm}^2}$), $\text{Ca}_0 = 2$ (mM), $D = 1$ (μm), $K_T = 0.0001$ (mM ms), and $K_d = 0.0001$ (mM). $F = 96.489$ ($\frac{\text{C}}{\text{mol}}$) is the Faraday constant, $R = 8.31441$ ($\frac{\text{J}}{\text{mol K}}$) is the universal gas constant, and the temperature T is set at 309.15 (K).

APPENDIX B: CPG PARAMETER VALUES

The numerical values of all the CPG parameters set following the proposed strategy are listed in Table III.

- [1] R. M. Harris-Warrick and J.-M. Ramirez, in *Neurobiology of Motor Control*, edited by S. L. Hooper and A. Büschges (John Wiley & Sons, Hoboken, NJ, 2017), Chap. 8, pp. 225–262.
- [2] C. Bellardita and O. Kiehn, *Curr. Biol.* **25**, 1426 (2015).
- [3] M. Lemieux, N. Josset, M. Roussel, S. Couraud, and F. Bretzner, *Front. Neurosci.* **10**, 42 (2016).
- [4] S. Grillner and A. Kozlov, *Int. J. Molec. Sci.* **22**, 5882 (2021).
- [5] T. G. Brown, *J. Physiol.* **48**, 18 (1914).
- [6] A. Hill, S. Hooser, and R. Calabrese, in *Handbook of Brain Theory and Neural Networks*, edited by M. A. Arbib (MIT Press, Cambridge, MA, 1998), pp. 444–447.
- [7] V. Baruzzi, M. Lodi, M. Storace, and A. Shilnikov, *Phys. Rev. E* **102**, 032406 (2020).
- [8] S. L. Jackman and W. G. Regehr, *Neuron* **94**, 447 (2017).
- [9] C. Gunaratne, A. Sakurai, and P. S. Katz, *J. Neurophysiol.* **118**, 1123 (2017).
- [10] S. M. Danner, S. D. Wilshin, N. A. Shevtsova, and I. A. Rybak, *J. Physiol.* **594**, 6947 (2016).
- [11] S. M. Danner, N. A. Shevtsova, A. Frigon, and I. A. Rybak, *Elife* **6**, e31050 (2017).
- [12] Y. I. Molkov, B. J. Bacak, A. E. Talpalar, and I. A. Rybak, *PLoS Comp. Biol.* **11**, e1004270 (2015).
- [13] M. Lodi, A. L. Shilnikov, and M. Storace, *IEEE Trans. Neural Netw. Learn. Syst.* **31**, 3658 (2020).
- [14] A. Destexhe, D. Contreras, T. J. Sejnowski, and M. Steriade, *J. Neurophysiol.* **72**, 803 (1994).
- [15] R. Nagornov, G. Osipov, M. Komarov, A. Pikovsky, and A. Shilnikov, *Commun. Nonlin. Sci.* **36**, 175 (2016).
- [16] X.-J. Wang and J. Rinzal, *Neural Comput.* **4**, 84 (1992).
- [17] X.-J. Wang, *Neuroscience* **89**, 347 (1999).
- [18] D. V. Buonomano, *J. Neurosci.* **20**, 1129 (2000).
- [19] S. Jalil, I. Belykh, and A. Shilnikov, *Phys. Rev. E* **85**, 036214 (2012).
- [20] D. Somers and N. Kopell, *Biol. Cybern.* **68**, 393 (1993).
- [21] M. Lodi, A. Shilnikov, and M. Storace, *IEEE Trans. Circ. Syst. I* **65**, 1028 (2017).
- [22] M. J. Giuliodori and G. Zuccolilli, *Adv. Physiol. Educ.* **28**, 79 (2004).
- [23] M. Lodi, A. Shilnikov, and M. Storace, in *Proceedings of the IEEE International Symposium on Circuits and Systems (ISCAS'17)* (IEEE, Los Alamitos, CA, 2017), pp. 1–4.
- [24] N. C. Heglund and C. R. Taylor, *J. Exp. Biol.* **138**, 301 (1988).
- [25] T. M. Griffin, R. Kram, S. J. Wickler, and D. F. Hoyt, *J. Exp. Biol.* **207**, 4215 (2004).
- [26] A. J. Ijspeert, *Neur. Netw.* **21**, 642 (2008).
- [27] J. Yu, M. Tan, J. Chen, and J. Zhang, *IEEE Trans. Neural Netw. Learn. Syst.* **25**, 441 (2013).
- [28] A. Lele, Y. Fang, J. Ting, and A. Raychowdhury, *IEEE Trans. Cogn. Develop. Syst.* (2021), doi: 10.1109/TCDS.2021.3097675.